

Sabina Ait ABDELKADER, Zhenpeng CUI, Abdelghani LAACHACHI, Christophe COLBEAU-JUSTIN, Mohamed Nawfal GHAZZAL

# Interfacial charge transfer and photocatalytic activity in a reverse designed Bi<sub>2</sub>O<sub>3</sub>/TiO<sub>2</sub> core-shell

© Higher Education Press 2021

**Abstract** In this study, the electronic and photocatalytic properties of core-shell heterojunctions photocatalysts with reversible configuration of TiO<sub>2</sub> and Bi<sub>2</sub>O<sub>3</sub> layers were studied. The core-shell nanostructure, obtained by efficient control of the sol-gel polymerization and impregnation method of variable precursors of semiconductors, makes it possible to study selectively the role of the interfacial charge transfer in each configuration. The morphological, optical, and chemical composition of the core-shell nanostructures were characterized by high-resolution transmission electron microscopy, UV-visible spectroscopy and X-ray photoelectron spectroscopy. The results show the formation of homogenous TiO<sub>2</sub> anatase and Bi<sub>2</sub>O<sub>3</sub> layers with a thickness of around 10 and 8 nm, respectively. The interfacial charge carrier dynamic was tracked using time resolved microwave conductivity and transition photocurrent density. The charge transfer, their density, and lifetime were found to rely on the layout layers in the core-shell nanostructure. In optimal core-shell design, Bi<sub>2</sub>O<sub>3</sub> collects holes from TiO<sub>2</sub>, leaving electrons free to react and increase by 5 times the photocatalytic efficiency toward H<sub>2</sub> generation. This study provides new insight into the importance of the design and elaboration of optimal heterojunction based on the photocatalyst system to improve the photocatalytic activity.

**Keywords** photocatalysis, core-shell, heterojunction, H<sub>2</sub>, TiO<sub>2</sub>, Bi<sub>2</sub>O<sub>3</sub>

## 1 Introduction

The decreasing of fossil resources and increasing environmental problems make it imperative to explore effective materials for clean and renewable energy conversion. Sunlight-driven photocatalytic hydrogen production from aqueous solution, as a credible solution for sustainable chemical fuel production, has attracted great research interests [1]. Metal oxides, whose stability is one of the driving force of these semiconductors, have become a very promising candidate for photocatalytic reactions [2].

TiO<sub>2</sub> is one of the most studied photocatalysts due to its suitable electronic and optical properties as well as good chemical stability [3]. However, despite the fact that its absorption is limited to the UV range (large band gap of 3–3.2 eV), the photoefficiency of TiO<sub>2</sub> for hydrogen production is very low, mainly due to the fast recombination of the photogenerated electron and hole (e<sup>-</sup>/h<sup>+</sup>). To tackle these issues, different approaches have been developed to mitigate this limitation with the aim to improve the photocatalytic hydrogen production. Coupling TiO<sub>2</sub> with co-catalysts has been extensively studied in the last decay and shows promising perspectives [4]. A wide range of co-catalysts, such as noble metals, low-cost metal ions/complexes, and metal-free materials have been coupled to TiO<sub>2</sub> to achieve efficient photocatalytic H<sub>2</sub> production [5–11]. The role of co-catalysts is variable regarding their localization on the active material [4]. Another interesting concept is to couple TiO<sub>2</sub> with semiconductors having variable potential band energy, adequately positioned (regarding to TiO<sub>2</sub>) [9,12]. This approach shows fair benefits and weaknesses. Metal sulfide shows both a narrow band gap and suitable disposition of the band energy [13,14]. Meanwhile, the generated holes are consumed to oxidize these materials,

Received Jan. 30, 2021; accepted Apr. 29, 2021; online Sept. 10, 2021

Sabina Ait ABDELKADER, Zhenpeng CUI, Christophe COLBEAU-JUSTIN, Mohamed Nawfal GHAZZAL (✉)

Université Paris-Saclay, UMR 8000, CNRS, Institut de Chimie Physique, Orsay 91405, France  
E-mail: mohamed-nawfal.ghazzal@universite-paris-saclay.fr

Abdelghani LAACHACHI

Materials Research and Technology Department (MRT), Luxembourg Institute of Science and Technology (LIST), Käerjeng 4940, Luxembourg

Special Issue—Photocatalysis: From Solar Light to Hydrogen Energy (Guest Editors: Wenfeng SHANGGUAN, Akihiko KUDO, Zhi JIANG, Yuichi YAMAGUCHI)

leading to a poor stability during the photocatalytic reaction [14]. Bismuth oxides coupled to TiO<sub>2</sub> offer instead a better stability and a promising photocatalytic efficiency for hydrogen generation [9,15–17]. Unlike transition metal oxides, the valence band (VB) of bismuth based semiconductors such as BiVO<sub>4</sub> or Bi<sub>2</sub>O<sub>3</sub> are composed of both O 2p and Bi 6s orbitals, which can increase the mobility of the charge carrier [18]. The higher mobility of the charge carrier goes with fast charge carrier recombination, which requires constructing a heterojunction. Moreover, bismuth vanadate has an unfavorable low-level CB flat-band energy to energetically initiate the reduction reactions, and consequently is photocatalytically inactive for the production of hydrogen. BiVO<sub>4</sub>/TiO<sub>2</sub> junction showed enhanced charge carriers separation for water splitting and a plausible photosensitization, via electron transfer from the conduction band (CB) of the BiVO<sub>4</sub> to the TiO<sub>2</sub>, under visible light illumination [19].

In this context, bismuth oxide has been identified as a stable semiconductor (SC) having a low band gap energy (2.29–3.31 eV depending on the crystalline phase [20]), whose flat-band potential are adequately positioned for electron and hole collection (likewise for BiVO<sub>4</sub>). Usually studied for water remediation either under UV or visible light [21,22], it has been recently reported that Bi<sub>2</sub>O<sub>3</sub>/TiO<sub>2</sub> junction is able to produce hydrogen from glycerol aqueous solution under UV illumination [15,23]. The mechanism proposed for the enhancement of the photocatalytic activity, often based on Type I classical electron charge separation in both SCs, is still ambiguous and needs further investigation, mainly due to the position of the respective conduction band of each SC and the arrangement of the adjacent photocatalysts. Furthermore, the charge transfer in heterojunctions remains an open question that should be investigated [24]. Indeed, the CB edge (CBE) is located just under the thermodynamic level for proton reduction to H<sub>2</sub> generation, thus the accumulation of electron from TiO<sub>2</sub> to Bi<sub>2</sub>O<sub>3</sub> makes the hydrogen ions reduction thermodynamically difficult.

In this study, tunable core-shell photocatalyst nanostructures based TiO<sub>2</sub>@Bi<sub>2</sub>O<sub>3</sub> junction are elaborated to study the effect of the core-shell system on the photocatalytic efficiency of hydrogen generation. The design of photocatalytic materials in core-shell nanostructures has been proven to be an original and efficient strategy to improve the photon conversion efficiency toward hydrogen generation [4,5]. The configuration of the system has been adjusted to make selectively accessible one of the two metal oxides at the surface for the photocatalytic reaction. For this purpose, silica nanoparticles were prepared as the core material supporting both TiO<sub>2</sub> or Bi<sub>2</sub>O<sub>3</sub> as a shell, depending on the configuration SiO<sub>2</sub>@TiO<sub>2</sub>@Bi<sub>2</sub>O<sub>3</sub> and SiO<sub>2</sub>@Bi<sub>2</sub>O<sub>3</sub>@TiO<sub>2</sub>. The novelty of this study compared to the reported studies [15,22,23] lies in the role played by the design of core-shell system and the available metal oxide at the surface. The highest photocatalytic H<sub>2</sub> generation was

observed for SiO<sub>2</sub>@Bi<sub>2</sub>O<sub>3</sub>@TiO<sub>2</sub> heterojunction (5.6 μmol/(g·min)), which was 7 and 13 times higher compared to SiO<sub>2</sub>@TiO<sub>2</sub>@Bi<sub>2</sub>O<sub>3</sub> (0.8 μmol/(g·min)) and SiO<sub>2</sub>@TiO<sub>2</sub> (0.4 μmol/(g·min)). The conduction and valence band edge position suggested a Type I for the interfacial charge transfer for SiO<sub>2</sub>@TiO<sub>2</sub>@Bi<sub>2</sub>O<sub>3</sub>, while there is a possibility of pseudo Type-II band alignment at the SiO<sub>2</sub>@Bi<sub>2</sub>O<sub>3</sub>@TiO<sub>2</sub> core/shell interface. It is suggested that the enhancement of the photocatalytic activity is attributed to the hole accumulation in Bi<sub>2</sub>O<sub>3</sub>, which increases the charge separation in TiO<sub>2</sub>, as evidenced by the time resolved microwave conductivity, the transition photocurrent density, and the photocatalytic hydrogen evolution.

## 2 Experiment

### 2.1 Chemicals

All the chemicals were of analytical grade and used directly without any further purification. They are tetraethyl orthosilicate (TEOS, Si(OC<sub>2</sub>H<sub>5</sub>)<sub>4</sub>, 98%, Sigma-Aldrich), ethanol (C<sub>2</sub>H<sub>5</sub>OH, ACS reagent, ≥99.8%), ammonium hydroxide (NH<sub>4</sub>OH, 28%), (3-aminopropyl) trimethoxysilane (APTMS, H<sub>2</sub>N(CH<sub>2</sub>)<sub>3</sub>Si(OCH<sub>3</sub>)<sub>3</sub>, 97%, Sigma-Aldrich), titanium (IV) isopropoxide (Ti(OiPr)<sub>4</sub>, TTIP, 97%, Sigma-Aldrich), bismuth(III) nitrate pentahydrate (Bi(NO<sub>3</sub>)<sub>3</sub>·5H<sub>2</sub>O, ≥98%, Sigma-Aldrich), methanol (CH<sub>3</sub>OH, ACS reagent, ≥99.8%). Deionized water (H<sub>2</sub>O, Millipore system, 18.2 MΩ·cm) was used to prepare the aqueous solutions.

### 2.2 Synthesis of reverse configuration of the core-shell nanostructure

#### 2.2.1 SiO<sub>2</sub> nanoparticles

SiO<sub>2</sub> nanoparticles were prepared following the procedures in Refs. [4,5]. Briefly, 17.1 mL of ethanol, 4.3 mL of NH<sub>3</sub> aqueous solution and 12.8 mL of H<sub>2</sub>O were mixed in a 250 mL glass bottle by stirring (500 rad/min). The bottle was sealed with a cap and the mixture was heated under stirring to 40°C. Then, 4.2 mL of TEOS was rapidly injected into the solution. The mixture was left to react under stirring for 1 h to form a colloidal suspension of monodisperse SiO<sub>2</sub> nanoparticles. After that, the SiO<sub>2</sub> nanoparticles were separated by centrifugation (5000 rad/min, 20 min), and washed three times with ethanol and deionized water. Finally, the powder was dried at 70°C for 24 h.

#### 2.2.2 Synthesis of SiO<sub>2</sub>@TiO<sub>2</sub> and SiO<sub>2</sub>@Bi<sub>2</sub>O<sub>3</sub> composites

The synthetic procedures of reverse configuration of the core-shell nanostructures were presented in Fig. 1. The

as-prepared  $\text{SiO}_2$  nanoparticles (200 mg) were added to 10 mL of ethanol under stirring, followed by sonication for 30 min for complete dispersion to avoid the aggregation of the nanoparticles. While the colloidal solution was stirred, 0.1 mL of APTMS was added to the dispersed solution dropwise and kept under stirring (500 rad/min) for 6 h at room temperature. The APTMS functionalized  $\text{SiO}_2$  nanoparticles were collected from the colloidal solution through centrifugation and washed three times with ethanol absolute.

The  $\text{SiO}_2@\text{TiO}_2$  was prepared as follows. APTMS functionalized  $\text{SiO}_2$  nanoparticles (200 mg) were added to a mixture of 20 mL of ethanol and 0.5 mL of  $\text{H}_2\text{O}$ . To disperse the functionalized  $\text{SiO}_2$  nanoparticles completely, sonication was performed for 30 min and the pH was adjusted at 12.4 using the  $\text{NH}_3$  aqueous solution. After stirring for 20 min, a mixture of 50 mL of ethanol and 1.5 mL of  $\text{Ti}(\text{OiPr})_4$  were added dropwise to the dispersed solution and left for 2 h under stirring (1000 rad/min) at room temperature. The coated colloidal  $\text{SiO}_2@\text{TiO}_2$  nanoparticles were separated by centrifugation, washed with ethanol several times, and dried at  $60^\circ\text{C}$  overnight.

Similarly,  $\text{Bi}_2\text{O}_3$  coated  $\text{SiO}_2$  nanoparticles were synthesized from the APTMS functionalized  $\text{SiO}_2$  nanoparticles, following the above procedure. Then, 0.5 g of  $\text{Bi}(\text{NO}_3)_3 \cdot 5\text{H}_2\text{O}$  was added into the colloidal solution. After sonication for 30 min, the mixture was stirred (500 rad/min) for 12 h. The product was separated by centrifugation (10000 rad/min), and washed several times with distilled water to remove the excess of the precursor. The  $\text{SiO}_2$  nanoparticles impregnated with  $\text{Bi}^{3+}$  were suspended in 10 mL of ethanol, sonicated for 10 min and then, the suspension was added dropwise to 40 mL ethanol (The pH was adjusted at 8.5). The solution was stirred during 2 h at ambient temperature, then at  $70^\circ\text{C}$  for 30 min. The as-prepared precipitate was separated through centrifugation, washed with ethanol and water several times,

and dried at  $60^\circ\text{C}$  overnight. The obtained core-shell nanoparticles were calcined at  $500^\circ\text{C}$  during 2 h.

### 2.2.3 Synthesis of $\text{SiO}_2@\text{TiO}_2@\text{Bi}_2\text{O}_3$ and $\text{SiO}_2@\text{Bi}_2\text{O}_3@\text{TiO}_2$ heterojunctions

For the synthesis of  $\text{SiO}_2@\text{TiO}_2@\text{Bi}_2\text{O}_3$  and  $\text{SiO}_2@\text{Bi}_2\text{O}_3@\text{TiO}_2$  composites, the as-prepared  $\text{SiO}_2@\text{TiO}_2$  and  $\text{SiO}_2@\text{Bi}_2\text{O}_3$  composites were further functionalized with the APTMS. By repeating the above synthetic procedures, the  $\text{SiO}_2@\text{TiO}_2$  composite was coated with  $\text{Bi}_2\text{O}_3$  while the  $\text{SiO}_2@\text{Bi}_2\text{O}_3$  composite was capped with the  $\text{TiO}_2$  layer. The core-shell heterojunctions were dried at  $60^\circ\text{C}$  overnight and calcined at  $500^\circ\text{C}$  for 2 h at a rate of  $2^\circ\text{C}/\text{min}$  under air.

## 2.3 Characterization

The optical properties were measured using diffuse reflectance spectroscopy (DRS) on a UV-vis-NIR spectrophotometer (Cary 5000 Series, Agilent Technologies) using a  $\text{BaSO}_4$  plate as reference.

The morphology of the as-prepared composites was studied by a transmission electron microscopy (TEM). The samples were dispersed in 2-propanol under sonication and deposited on a holey carbon-coated copper grid (Quantifoil Micro Tools GmbH, Großlobichau, Germany). The typical TEM images were collected by a JEOL JEM 2100 Plus CXII equipped with LaB6 filament microscope, operating at 100 kV, and the images were collected with a  $4008 \times 2672$  pixels CCD camera (Gatan Orius SC1000). The X-ray photoelectron spectroscopies (XPS) of different core-shell heterojunctions were obtained on an ESCALAB 250 spectrophotometer with  $\text{Al-K}\alpha$  radiation. The binding energies were calibrated using C 1s at 284.8 eV. Bragg-Brentano X-ray diffraction (XRD) measurements were performed on an Aeris Malvern Panalytical diffractometer

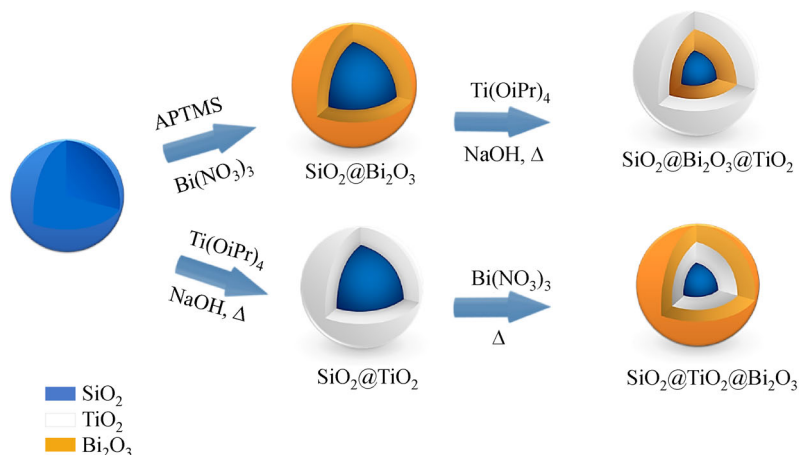


**Fig. 1** Schematic representation of the synthesis of core-shell heterojunctions.

using Ni filtered Cu K<sub>α1</sub> radiation (1.540598 Å) from 10° to 70° with a step size of 0.022° and a counting time of 29.070 s per step. The K<sub>α2</sub> radiation (1.544426 Å) was mathematically stripped.

The dynamics of photogenerated charge carriers in the composite under UV light ( $\lambda = 360$  nm) irradiation was studied by time-resolved microwave conductivity (TRMC) method. The TRMC technique used a pulsed laser source with an optical parametric oscillator (OPO; EKSPLA, NT342B), tunable in the range of 200–2000 nm. The full width at half-maximum of one pulse was 8 ns, the repetition frequency of the pulses was 10 Hz, and microwaves were generated with a Gunn diode (30 GHz). The principle of this technique was described in detail in Refs. [11,25]. In brief, the TRMC measurement of the microwave power reflected by a semiconductor sample are monitored when it is irradiated by a nanosecond pulsed laser. The signal obtained by the diode detector is correlated to voltage for input to the oscilloscope following Eq. (1).

$$\frac{\Delta P(t)}{P} = A\Delta\sigma(t) = A\mu_i\Delta n_i(t), \quad (1)$$

where  $\Delta P$  is the microwave power absorbed by the sample,  $A$  is independent of time but depends on the microwave frequency and the conductivity of the sample,  $\Delta\sigma(t)$  is the conductance,  $\Delta n_i(t)$  is the number of excess charge carriers  $i$  at time  $t$ , and  $\mu_i$  is the mobility of the charge carriers. The TRMC signal reflects the number of mobile charge carriers created right after the laser pulse excitation, the charge carriers lifetime (decay processes) during the excitation, and the decay of the signal due to the decrease of excess electrons controlled by recombination, trapping or surface reaction.

Photoelectrochemical measurements were performed in a three-electrode cell in 0.1 mol/L Na<sub>2</sub>SO<sub>4</sub> solution under simulated sunlight illumination (AM 1.5 G, 100 mW/cm<sup>2</sup>). An electrochemical workstation Orignalyx (France) was used to record the current. A counter electrode of platinum disk and an Ag/AgCl electrode (3 mol/L KCl) were used as the reference ( $E_{\text{RHE}} = E_{\text{Ag/AgCl}} + 0.197 + 0.059 \text{ pH}$ ). The electrolyte was degassed for 15 min by flushing N<sub>2</sub> prior to each measurement. The working electrodes were prepared by spreading the target solution (1 mg/mL) on a fluorine-doped tin oxide (FTO) glass substrate with an active area of about 1 cm<sup>2</sup>, and then the film was dried at room temperature.

#### 2.4 Photocatalytic hydrogen production

The photocatalytic production of H<sub>2</sub> was assessed during a standard test, a mixture solution of methanol and water ( $v_m/v_w = 25/75$ ) with a total volume of 20 mL was added into a quartz reactor, and 20 mg of composite photocatalyst

was added under vigorous stirring. Then, the reactor was sealed and degassed with nitrogen (N<sub>2</sub>) for 30 min to remove dissolved oxygen. Methanol is used as a hole scavenger and sacrificial electron donor. The photocatalyst was dispersed in the solution at a concentration of 1 mg/mL. A Xenon lamp (300 W) was used as light sources and the amount of H<sub>2</sub> produced as a function of irradiation time was monitored by a gas chromatography (GC, Agilent 7280A system) with a thermal conductivity detector (oven temperature, 70°C; detector temperature, 200°C; carrier gas, N<sub>2</sub>).

## 3 Results

### 3.1 Morphological properties and surface chemical analysis

The morphology of the SiO<sub>2</sub>@TiO<sub>2</sub> core-shell nanostructures was observed by TEM and the typical images are presented in Fig. 2. The TEM images, through contrast difference between the core and the shell, evidence the success of the coating procedure used based on the polycondensation of the TTIP precursor under the basic condition. APTMS functionalized silica core provides a nucleation site for homogenous growth of the TiO<sub>2</sub> at the surface of the SiO<sub>2</sub>. Thus, the polycondensation of TiO<sub>2</sub> leads to the formation of a thin layer, covering the silica surface, whose size is estimated to range from 60 to 90 nm (Fig. 2(a)). The thickness of the shell is estimated to be in the range of 5–8 nm (Fig. 2(b)).

The images of the core-shell nanoparticles, demonstrated in Figs. 2(c) and 2(d), indicate that the spherical shape is maintained after both Bi<sub>2</sub>O<sub>3</sub> and TiO<sub>2</sub> are coated. The coating procedure makes it possible to adsorb Bi<sup>3+</sup> ions at the surface of silica nanoparticles under the basic condition. Bismuth ions are not stable and react with hydroxyl groups to form Bi<sub>2</sub>O<sub>3</sub> [26]. The surface of the nanoparticles, after the TiO<sub>2</sub> layer growth, appears with a higher roughness and the contrast between metal oxides is less obvious compared to SiO<sub>2</sub>@TiO<sub>2</sub> nanoparticles, probably because of the increase of the thickness of the shell of the two metal oxides. The fast Fourier transform pattern of selected area revealed (211) face of TiO<sub>2</sub> anatase with an interplanar spacing of 1.71 nm (inset Fig. 2(c)). The HR-TEM results depicted in Fig. 2(d) indicate that the lattice fringes with d-spacing of 0.351 nm are consistent with the (101) TiO<sub>2</sub> anatase crystallographic plane. Further TEM analysis of SiO<sub>2</sub>@TiO<sub>2</sub>@Bi<sub>2</sub>O<sub>3</sub> show the success of the core-shell nanostructure and the well deposited Bi<sub>2</sub>O<sub>3</sub> at the surface (Figs. 2(e) and 2(f)).

The crystalline structures of the as-prepared samples were identified by XRD and the results are displayed in Fig. 3. It is clearly observed that SiO<sub>2</sub>@TiO<sub>2</sub> samples exhibit an anatase phase with (101) preferential orientation. The XRD patterns of SiO<sub>2</sub>@BiO<sub>2</sub> indicates the

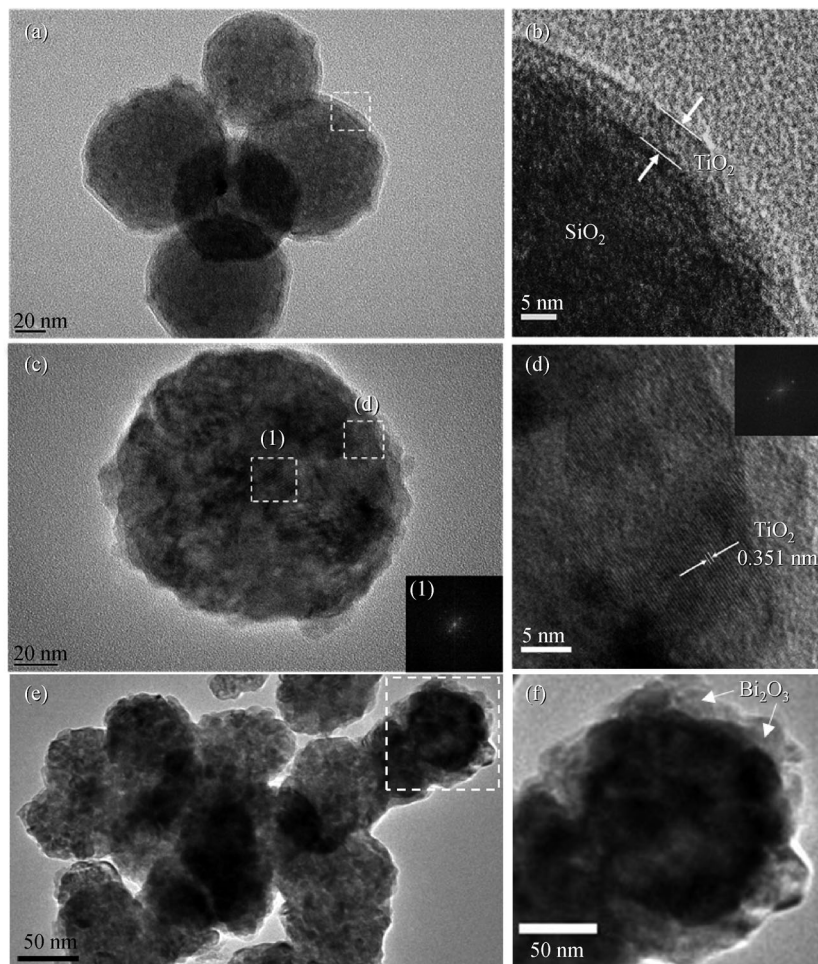


**Fig. 2** TEM images.

(a)  $\text{SiO}_2@\text{TiO}_2$ ; (b) enlargement of selected region in (a); (c)  $\text{SiO}_2@\text{Bi}_2\text{O}_3@\text{TiO}_2$  core-shell nanospheres; (d) high magnification of the selected region in (c); (e)  $\text{SiO}_2@\text{TiO}_2@\text{Bi}_2\text{O}_3$  core-shell nanospheres; (f) high magnification of the selected region in (e) showing  $\text{Bi}_2\text{O}_3$  shell.

existence of crystalline  $\text{Bi}_2\text{O}_3$ . Core-shell nanostructure for reverse configuration,  $\text{SiO}_2@\text{TiO}_2@\text{Bi}_2\text{O}_3$  and  $\text{SiO}_2@\text{Bi}_2\text{O}_3@\text{TiO}_2$ , present both crystalline structure of  $\text{TiO}_2$  anatase and  $\text{Bi}_2\text{O}_3$  as evidenced in Fig. 3.

Surface analysis of  $\text{SiO}_2@\text{TiO}_2$  and  $\text{SiO}_2@\text{TiO}_2@\text{Bi}_2\text{O}_3$  has been carried out using XPS to determine the chemical composition of the outer surface composition of the photocatalyst ( $\text{Bi}_2\text{O}_3$  or  $\text{TiO}_2$ ), as displayed in Fig. 4. General survey of the surface of  $\text{SiO}_2@\text{TiO}_2$  core-shell is depicted in Fig. 4(a). The results indicate that the surface is mainly composed of four elements, i.e., C, O, Si, and Ti, in which the concentration of each element is 18%, 9.5%, 60.5% and 11.5%, respectively. The presence of Si elements is due to the thinness of the shell (measured to be in the range of 5–8 nm). XPS analyses the surface up to approximately 8 nm, which means that the silica core is also detected. Furthermore, during the calcination step, a diffusion of Si could occur from the core to the shell [27]. The Si 2p region shows a peak centered at that correspond

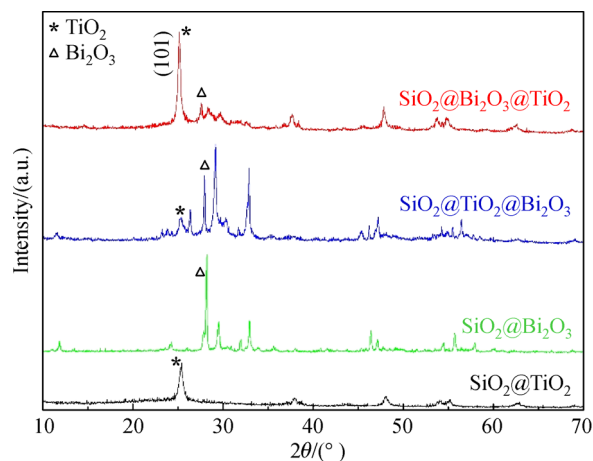


**Fig. 3** X-ray diffractograms of different core-shell nanostructures.

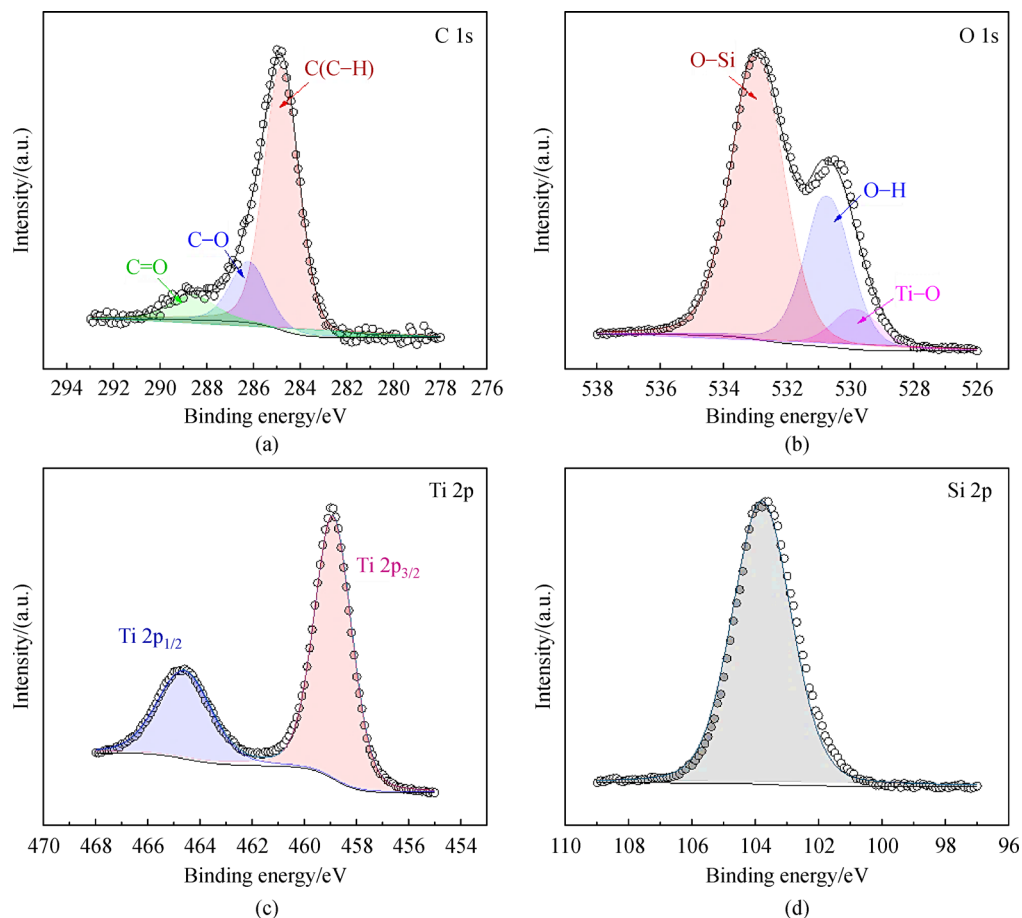


**Fig. 4** XPS profile of SiO<sub>2</sub>@TiO<sub>2</sub> core-shell nanostructure. (a) C 1s; (b) O 1s; (c) Ti 2p; (d) Si 2p.

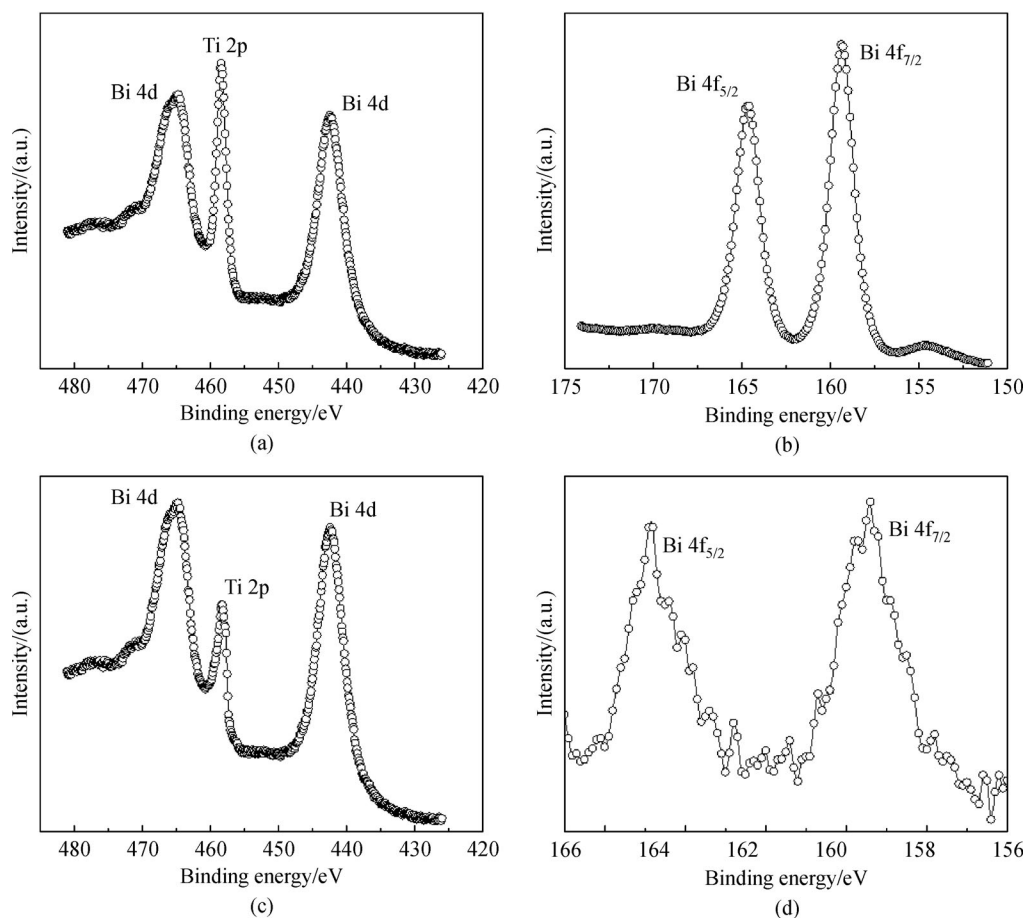
to elemental silicon and silicon dioxide. The C 1s peak at the binding energy (BE) value of 284.8 eV is attributed to hydrocarbon mostly related to the residual carbon resulting from the decomposition of the titanium precursor and some surface contamination during the XPS analysis. The O 1s peak could be deconvoluted into three peaks at 529.8, 530.7, and 532.2 eV. These peaks could be assigned to oxygen binding to variable elements such as titanium and silicon, hydrogen of the hydroxyl groups and to carbon. The spin-orbit components of the Ti 2p<sub>3/2</sub> and Ti 2p<sub>1/2</sub> peaks were usually deconvoluted into two curves, each at the BE of 458.9 and 464.6 eV, respectively. The separation measured between the maximum of the peaks (5.7 eV) is in agreement with the binding energy separation observed for TiO<sub>2</sub> anatase [28].

Figure 5 presents the Ti 2p and Bi 4f XPS profiles of SiO<sub>2</sub>@Bi<sub>2</sub>O<sub>3</sub>@TiO<sub>2</sub> and SiO<sub>2</sub>@TiO<sub>2</sub>@Bi<sub>2</sub>O<sub>3</sub>, and SiO<sub>2</sub>@Bi<sub>2</sub>O<sub>3</sub> samples, respectively. The results demonstrate that in addition to the Ti element, Bi is also detected in both core-shell reverse configuration samples. An overlap of the peaks of Ti 2p and Bi 4d states are observed. The ratio of Ti is higher for the SiO<sub>2</sub>@Bi<sub>2</sub>O<sub>3</sub>@TiO<sub>2</sub>

sample compared to SiO<sub>2</sub>@TiO<sub>2</sub>@Bi<sub>2</sub>O<sub>3</sub>, as evidenced by XPS (Figs. 5(a) and 5(c)). The presence of Ti elements for SiO<sub>2</sub>@TiO<sub>2</sub>@Bi<sub>2</sub>O<sub>3</sub> provides information about the thickness of the Bi<sub>2</sub>O<sub>3</sub> shell, which should be thinner than 8 nm (as the depth limit analyzed by XPS is up to 8 nm). These results complement the TEM analysis, providing an evidence of the successful coating of the SiO<sub>2</sub>@TiO<sub>2</sub> core-shell by the Bi<sub>2</sub>O<sub>3</sub> thin overlayer. In addition, the Bi 4f<sub>7/2</sub> and Bi 4f<sub>5/2</sub> asymmetric bands are located at the BE at 159.4 and 164.7 eV for all samples, respectively. These orbitals and the separation of 5.3 eV correspond to Bi<sup>3+</sup> oxide state in pure SiO<sub>2</sub>@Bi<sub>2</sub>O<sub>3</sub> (Fig. 5(d)), in agreement with Refs. [17,29,30].

### 3.2 Optical properties

The optical properties were evaluated by recording the UV-visible absorbance spectra of the composites core-shell in the range of 250–800 nm and the results are presented in Fig. 6. As manifested in Fig. 6(a), SiO<sub>2</sub>@TiO<sub>2</sub> displays an absorption in the UV range starting from 360 nm, which corresponds to the presence of TiO<sub>2</sub> nanoparticles in its



**Fig. 5** Ti 2p and Bi 4f XPS profiles.  
(a, b)  $\text{SiO}_2@Bi_2O_3@TiO_2$ ; (c)  $\text{SiO}_2@TiO_2@Bi_2O_3$ ; (d)  $\text{SiO}_2@Bi_2O_3$ .

anatase form [31]. Compared to  $\text{SiO}_2@TiO_2$  nanoparticles, the coating core-shell nanostructure with  $Bi_2O_3$  shift the absorption band edge in the visible range. The  $\text{SiO}_2@Bi_2O_3$  composite with an absorption edge starting at 550 nm in the visible range is blue-shifted when a  $TiO_2$  layer is coated at the surface. As a result, the  $\text{SiO}_2@Bi_2O_3@TiO_2$  composite shows a band edge absorption starting at 420 nm. Likewise, coating the top of  $\text{SiO}_2@TiO_2$  with  $Bi_2O_3$  red shift the absorbance edge to 540 nm.

The optical bandgap ( $E_g$ ) of the nanocomposites were determined using a Tauc plot of modified Kubelka-Munk (KM) function with a linear extrapolation (Fig. 6(b)). The titanium dioxide in the  $\text{SiO}_2@TiO_2$  sample operates with a bandgap energy of 3.65 eV. This value is in agreement with the one reported for small sized  $TiO_2$  anatase supported on silica substrate [31,32]. Indeed, the diffusion of the Si element from the silica or the compressive residual stress inhibit the growth of  $TiO_2$ , leading to the small crystallite size. The energy of the bandgap of  $\text{SiO}_2@Bi_2O_3$  was 2.21 eV, which is consistent with the bismuth oxide material [33]. The composites  $\text{SiO}_2@TiO_2@Bi_2O_3$  and  $\text{SiO}_2@$ -

$Bi_2O_3@TiO_2$  showed intermediate bandgap energies of 2.29 eV and 3.17 eV, respectively, which was caused by the existence of  $TiO_2$ .

### 3.3 Charge carriers dynamics and transition photoresponse of core-shell heterojunctions

The electronic properties of the core-shell heterojunction were studied by means of TRMC as a contactless technique under UV excitation. The TRMC makes it possible to conduct fast photoconductivity measurements to determine the charge carrier mobility and transfer, charge carrier density, and subsequent decay. The signal rising in the first 20 ns is caused by the instrumental response time and the width of the laser pulse. This is followed by a decay, due to a decrease of the density of free charges. Figure 7(a) shows the typical TRMC signal for  $\text{SiO}_2@TiO_2$ ,  $\text{SiO}_2@TiO_2@Bi_2O_3$  and  $\text{SiO}_2@Bi_2O_3@TiO_2$  core-shell heterojunction after their illumination by the laser pulse emitting at 360 nm. The signal rises from the interaction of the electric field component of the microwaves with mobile charges

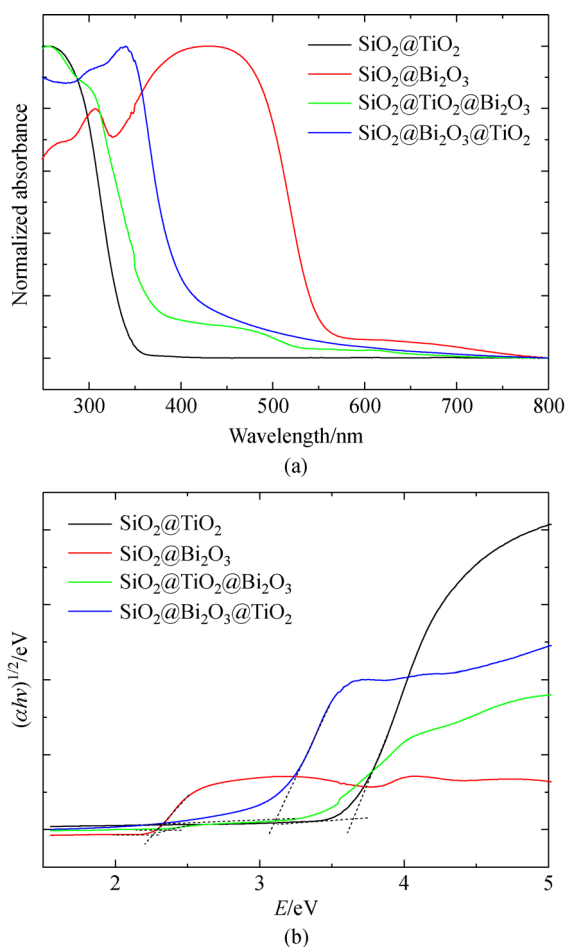


**Fig. 6** Optical characterization of variable core-shell systems. (a) UV-visible diffuse reflectance spectra of TiO<sub>2</sub> based core-shell structured composite; (b) plot of transformed Kubelka-Munk function  $(\alpha hv)^{1/2}$  vs  $E = hv$  (eV).

produced after illumination in the bulk of the photocatalyst, resulting in a change in the real and imaginary conductance [34]. The signal relies mainly on electrons that are more mobile than holes. The results showed different charge carrier density produced after illumination for each samples. The electron density for the SiO<sub>2</sub>@TiO<sub>2</sub> nanostructure was found to be very low due to the thinness of TiO<sub>2</sub> photoactive shell or the small crystallite size. As soon as photogenerated electron/hole pairs are produced, they either recombine or are trapped by the surface defects, leading to the nearly zero TRMC signal. The TRMC signal can be divided into three decay stages: charge trapping ( $\tau_{\text{trap}}$ ), charge recombination ( $\tau_{\text{rec}}$ ), and surface reactions ( $\tau_{\text{surf}}$ ) [11]. The trapping time of electrons and holes occurs in an early time (30 ps), and it is accompanied by the fast recombination, occurred during the laser pulse. Both of the trapping and recombination phenomena are considered as the main processes that can explain the decay of the TRMC signals, since the surface reaction occurs at a longer time. During the coupling of TiO<sub>2</sub> and Bi<sub>2</sub>O<sub>3</sub>, it has been found that the mobility of electrons is sensitive to the design of

the core-shell heterojunction nanostructure. The TRMC signal of SiO<sub>2</sub>@Bi<sub>2</sub>O<sub>3</sub> is shown in Fig. A1. The results suggest that the decay of the TRMC signals, related to the photocharges, is much faster compared to SiO<sub>2</sub>@Bi<sub>2</sub>O<sub>3</sub>@TiO<sub>2</sub> core-shell. The time constant of electron trapping and recombination can be quantitatively estimated to be  $\tau_{\text{trap}} = 0.0815 \mu\text{s}$ ,  $\tau_{\text{rec}} = 0.51296 \mu\text{s}$  and  $\tau_{\text{surf}} = 0.51328 \mu\text{s}$ , which are faster compared to  $\tau_{\text{trap}} = 0.12643 \mu\text{s}$ ,  $\tau_{\text{rec}} = 0.12729 \mu\text{s}$  and  $\tau_{\text{surf}} = 1.93922 \mu\text{s}$  for SiO<sub>2</sub>@Bi<sub>2</sub>O<sub>3</sub>@TiO<sub>2</sub> core-shell. The fast recombination of photogenerated charge carriers of SiO<sub>2</sub>@Bi<sub>2</sub>O<sub>3</sub> leads to a very low photocurrent as evidenced in Fig. A1(b). The insertion of Bi<sub>2</sub>O<sub>3</sub> between the silica core and the TiO<sub>2</sub> shell leads to an increase of the charge carrier density. Meanwhile, using Bi<sub>2</sub>O<sub>3</sub> as the outer layer shows a small but sensitively higher electron density production and mobility compared to the SiO<sub>2</sub>@TiO<sub>2</sub> sample. The results suggest that efficient charge carrier separation and transfer operate regarding the disposition of the layers.

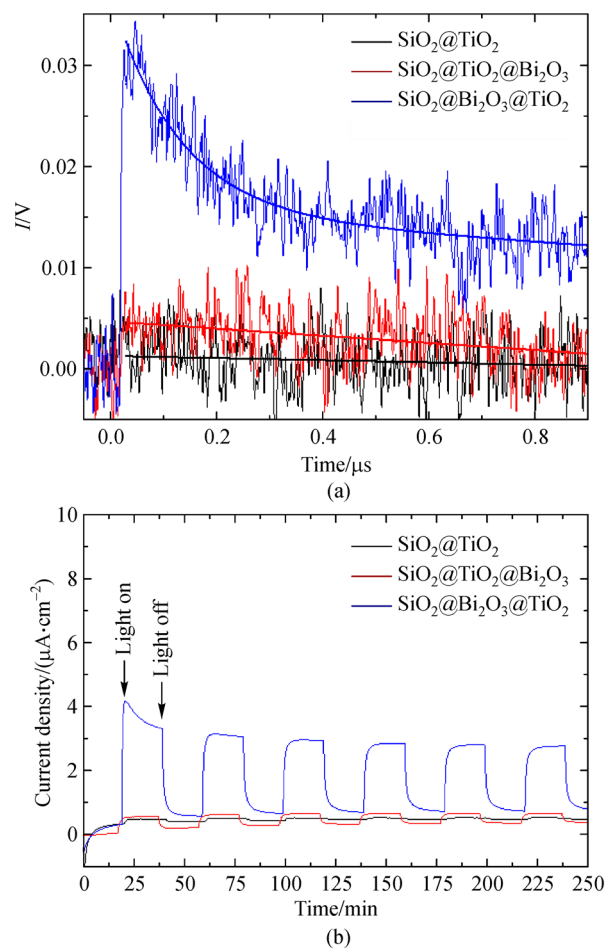


**Fig. 7** Charge carriers dynamic and photocurrent response of variable core-shell photocatalysts. (a) TRMC measurements recorded under UV excitation ( $\lambda = 360 \text{ nm}$ ,  $I_{\text{ex}} = 1.6 \text{ mJ/cm}^2$ ); (b) transient photocurrent responses under UV-visible simulated sunlight illumination (AM 1.5 G,  $100 \text{ mW/cm}^2$ ).

The photocurrent-time response of the core-shell nanostructures in on/off cycles under solar light irradiation was further investigated and the results are presented in Fig. 7(b). It can be observed that there was a remarkable increase of the photocurrent when the irradiation was turned on. However, the photocurrent value rapidly decreased as soon as the irradiation was turned off. Combining  $\text{Bi}_2\text{O}_3$  and  $\text{TiO}_2$  in the core-shell heterojunction exhibited an enhanced photocurrent compared to  $\text{SiO}_2@\text{TiO}_2$ , whose photoresponse is very low ( $0.14 \mu\text{A}$ ). The photocurrent density of  $\text{SiO}_2@\text{Bi}_2\text{O}_3@\text{TiO}_2$  ( $2.6 \mu\text{A}/\text{cm}^2$ ) was about 5.2 times higher than that induced in  $\text{SiO}_2@\text{TiO}_2@\text{Bi}_2\text{O}_3$  ( $0.54 \mu\text{A}/\text{cm}^2$ ) under solar light irradiation. These results, in agreements with the TRMC signal, indicate that the layout layers are crucial for optimal charge carrier separation and mobility.

### 3.4 Photocatalytic $\text{H}_2$ generation

The photocatalytic efficiency of the as-prepared core-shell heterojunctions was assessed for hydrogen production from methanoic aqueous solution ( $\text{MeOH}/\text{H}_2\text{O}$ : 25/75) under UV-visible illumination and presented in Fig. 8(a). In the dark condition, the hydrogen production was not observed. Under UV-visible illumination,  $\text{SiO}_2@\text{Bi}_2\text{O}_3$  does not reveal any detectable hydrogen generation. Once coupled to  $\text{TiO}_2$  in the core-shell nanostructure, the heterojunction showed variable behaviors toward the hydrogen generation. The highest photocatalytic  $\text{H}_2$  generation was observed for  $\text{SiO}_2@\text{Bi}_2\text{O}_3@\text{TiO}_2$  heterojunction ( $5.6 \mu\text{mol}/(\text{g}\cdot\text{min})$ ), which was 7 and 13 times higher compared to  $\text{SiO}_2@\text{TiO}_2@\text{Bi}_2\text{O}_3$  ( $0.8 \mu\text{mol}/(\text{g}\cdot\text{min})$ ) and  $\text{SiO}_2@\text{TiO}_2$  ( $0.4 \mu\text{mol}/(\text{g}\cdot\text{min})$ ), respectively, as shown in Fig. 8(b). This result suggests that the  $\text{Bi}_2\text{O}_3$  alone is not able to produce hydrogen, but it contributes to the enhancement of the photoactivity of  $\text{TiO}_2$ . More importantly, the synergetic effect between  $\text{Bi}_2\text{O}_3$  and  $\text{TiO}_2$  depends on their order on the core-shell heterojunction. These results are in agreement with the TRMC and transition photocurrent results, which is also a correlated to the layout orders of both semiconductors in the core-shell nanostructure.

## 4 Discussion

The experimental results show that the most active core-shell heterojunction for  $\text{H}_2$  generation also showed both the optimal charge carrier separation and the highest photocurrent density. More importantly, these results were dependent on the layout layers of  $\text{TiO}_2/\text{Bi}_2\text{O}_3$  in the core-shell nanostructure. To understand the occurrence of the charge carrier transfer in  $\text{TiO}_2/\text{Bi}_2\text{O}_3$  core-shell heterojunction, the valence band and conduction band energies were determined. In heterojunction structures, it is crucial

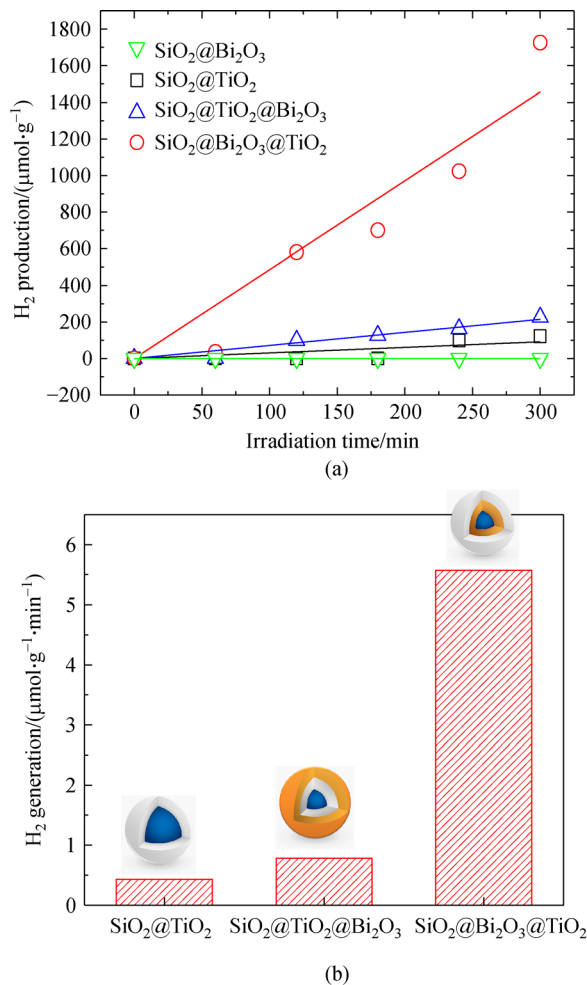


**Fig. 8** Photocatalytic characterization of different core-shell heterojunctions during UV-visible irradiation.

(a) Photocatalytic  $\text{H}_2$  generation; (b)  $\text{H}_2$  production rate.

to identify the highest occupied and the lowest unoccupied electronic levels in each semiconductor. For  $\text{H}_2$  evolution, the conduction band (CB) edge should be more negative than the reduction potential of  $\text{H}^+$  to  $\text{H}_2$  ( $E_{\text{H}^+/\text{H}_2} = 0 \text{ V}$  versus NHE at  $\text{pH} = 0$ ). Thus, knowing the optical bandgap energy, obtained from UV-visible DRS spectra, the highest occupied electronic level of the top of the VB and the lowest unoccupied electronic level of the CB of both  $\text{TiO}_2$  and  $\text{Bi}_2\text{O}_3$  can be predicted using the relationship between band edge energies and electronegativity [33] in Eqs. (2) and (3).

$$E_{\text{VB}} = X - E^e + 0.5E_g^e, \quad (2)$$

$$E_{\text{CB}} = X - E^e - 0.5E_g^e, \quad (3)$$

where  $X$  is the absolute electronegativity of each semiconductor and defined as the geometric mean of the absolute electronegativity of constituent atoms ( $X$  values

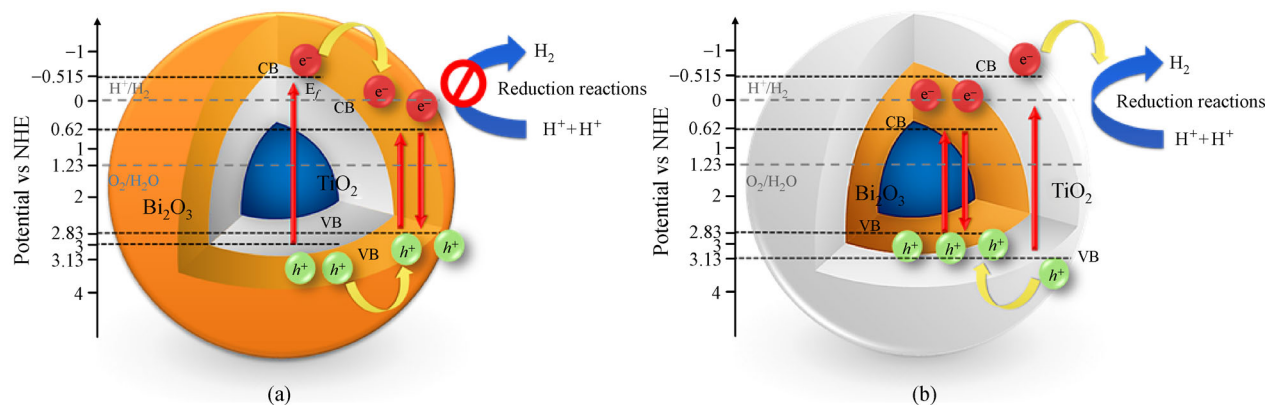


**Fig. 9** Diagram of band energy and possible charge separation process for core-shell heterojunctions systems. (a) SiO<sub>2</sub>@TiO<sub>2</sub>@Bi<sub>2</sub>O<sub>3</sub>; (b) SiO<sub>2</sub>@Bi<sub>2</sub>O<sub>3</sub>@TiO<sub>2</sub>.

for TiO<sub>2</sub> and Bi<sub>2</sub>O<sub>3</sub> are 5.81 and 6.23 eV, respectively [33]),  $E^e$  is the energy of free electrons on the hydrogen scale (approximately 4.5 eV),  $E_{VB}$  is the VB edge potential,  $E_{CB}$  is the CB edge potential, and  $E_g$  is the bandgap energy for each semiconductor obtained from the UV-visible DRS. The top of the VB and the bottom of the CB of TiO<sub>2</sub> and Bi<sub>2</sub>O<sub>3</sub> were 2.83/0.62 eV and 3.13/−0.515 eV, respectively (Figs. 9(a) and 9(b)). The inability of SiO<sub>2</sub>@Bi<sub>2</sub>O<sub>3</sub> to produce hydrogen is related to the fact that the bottom of the CB of Bi<sub>2</sub>O<sub>3</sub> stands at a higher energy than the redox potential of hydrogen. After irradiation of the SiO<sub>2</sub>@TiO<sub>2</sub>@Bi<sub>2</sub>O<sub>3</sub>, the photogenerated charge carrier ( $e^-/h^+$ ) would thermodynamically transfer from TiO<sub>2</sub> to Bi<sub>2</sub>O<sub>3</sub> following Type-I band alignment of the core-shell interface, which would prolong the lifetimes of the electrons and then promote the interfacial charge separation (Fig. 9(a)). The charge carrier separation explains very well the increase of both the TRMC signal and the photocurrent density measured for SiO<sub>2</sub>@TiO<sub>2</sub>@Bi<sub>2</sub>O<sub>3</sub>, compared to the solely SiO<sub>2</sub>@TiO<sub>2</sub>. The small increase of the production of hydrogen for this sample could result from the diffusion of energetic electrons produced at the TiO<sub>2</sub> layer, since the bottom CB energy makes Bi<sub>2</sub>O<sub>3</sub> thermodynamically unable to reduce hydrogen because the potential of the  $e^-$  in the CB of Bi<sub>2</sub>O<sub>3</sub> is more positive than the standard redox potential of hydrogen. When the disposition of core-shell heterojunction was changed (SiO<sub>2</sub>@Bi<sub>2</sub>O<sub>3</sub>@TiO<sub>2</sub>), making TiO<sub>2</sub> the outer layer, an impressive hydrogen generation was observed. The charge carriers in this system are spatially separated in two semiconductors.

Therefore, there is a possibility of pseudo Type-II band alignment at the core/shell interface, where the hole is delocalized over both the shell and core, and the electron is localized outside the shell (Fig. 9(b)). The photogenerated holes produced at the TiO<sub>2</sub> VB band are accumulated in the Bi<sub>2</sub>O<sub>3</sub> VB band, since the bottom of the CB stands at about −0.515 eV versus NHE, leaving the electron at the TiO<sub>2</sub> surface to reduce H<sup>+</sup> to H<sup>•</sup> efficiently. In this case, Bi<sub>2</sub>O<sub>3</sub>

acts as a hole transfer layer, favoring the increase of the electron density (TRMC signal and transition photoelectron density) at the TiO<sub>2</sub> surface.

## 5 Conclusions

In this work, core-shell heterojunctions were prepared by depositing alternatively TiO<sub>2</sub> and Bi<sub>2</sub>O<sub>3</sub> by successive sol-gel polycondensation and adsorption precipitation steps. The design of such core-shell heterojunction made it possible to assess selectively the optical, electronic, and photocatalytic properties of the outer layer, i.e., TiO<sub>2</sub> or Bi<sub>2</sub>O<sub>3</sub>. The best configuration of the core-shell heterojunction was found when Bi<sub>2</sub>O<sub>3</sub> was coated with TiO<sub>2</sub>. The interfacial charge transfer was found to be affected by the reverse core-shell configuration. The charge carrier transfer for SiO<sub>2</sub>@TiO<sub>2</sub>@Bi<sub>2</sub>O<sub>3</sub> followed Type-I band alignment of the core-shell interface. In the reverse configuration, the separation of charge carriers as well as the photocurrent density and the photocatalytic efficiency were found to be promoted when Bi<sub>2</sub>O<sub>3</sub> was deposited below TiO<sub>2</sub>, favoring a pseudo-Type II band alignment, as demonstrated by the TRMC and transition photocurrent measurements. Following the disposition of the VB and CB energy of each layer, holes were accumulated in Bi<sub>2</sub>O<sub>3</sub> layer leaving electrons free to react for the reduction reaction of hydrogen. The photocatalytic H<sub>2</sub> generation was observed to increase by 7 and 13 times for SiO<sub>2</sub>@Bi<sub>2</sub>O<sub>3</sub>@TiO<sub>2</sub> compared to SiO<sub>2</sub>@TiO<sub>2</sub>@Bi<sub>2</sub>O<sub>3</sub> and SiO<sub>2</sub>@TiO<sub>2</sub>. This approach can be extended to study the charge carriers transfer in other semiconductors and selectively assess the role playing by each material in order to optimize the efficiency of heterojunctions.

**Acknowledgements** This work was supported by the public grant overseen by the French National Research Agency (ANR) as part of the “Investissements d’Avenir” program (Labex NanoSaclay, reference: ANR-10-LABX-0035) through project “Z-scheme,” the “Agence Nationale de la Recherche (ANR)” through the UpPhotoCat project, and the “Département de Chimie de

la Faculté des Sciences d'Orsay de l'Université Paris-Saclay" through young researcher grant.

## Appendix

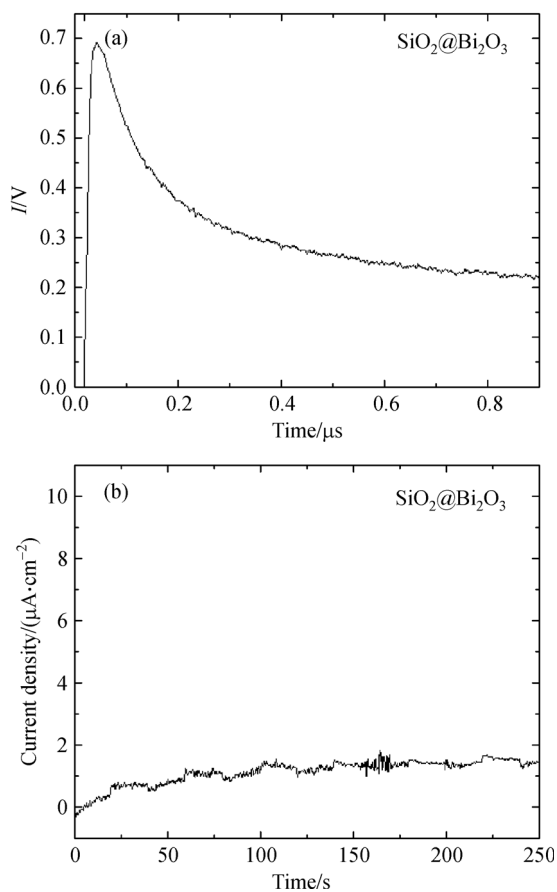


**Fig. A1** Charge carriers dynamic and photocurrent response under UV-visible simulated sunlight illumination (AM 1.5 G, 100 mW/cm<sup>2</sup>) for SiO<sub>2</sub>@Bi<sub>2</sub>O<sub>3</sub> core-shell.

(a) TRMC signals; (b) transient photocurrent response.

## References

- Kumaravel V, Mathew S, Bartlett J, et al. Photocatalytic hydrogen production using metal doped TiO<sub>2</sub>: a review of recent advances. *Applied Catalysis B: Environmental*, 2019, 244: 1021–1064
- Reza Gholipour M, Dinh C T, Béland F, et al. Nanocomposite heterojunctions as sunlight-driven photocatalysts for hydrogen production from water splitting. *Nanoscale*, 2015, 7(18): 8187–8208
- Ghazzal N M, Chaoui N, Aubry E, et al. A simple procedure to quantitatively assess the photoactivity of titanium dioxide films. *Journal of Photochemistry and Photobiology A Chemistry*, 2010, 215(1): 11–16
- Gesesse G D, Wang C, Chang B K, et al. A soft-chemistry assisted strong metal–support interaction on a designed plasmonic core–shell photocatalyst for enhanced photocatalytic hydrogen production. *Nanoscale*, 2020, 12(13): 7011–7023
- Gesesse G D, Le Neel T, Cui Z, et al. Plasmonic core-shell nanostructure as an optical photoactive nanolens for enhanced light harvesting and hydrogen production. *Nanoscale*, 2018, 10(43): 20140–20146
- Liu M, Inde R, Nishikawa M, et al. Enhanced photoactivity with nanocluster-grafted titanium dioxide photocatalysts. *ACS Nano*, 2014, 8(7): 7229–7238
- Liu G, Du K, Haussener S, et al. Charge transport in two-photon semiconducting structures for solar fuels. *ChemSusChem*, 2016, 9(20): 2878–2904
- Naldoni A, Altomare M, Zoppellaro G, et al. Photocatalysis with reduced TiO<sub>2</sub>: from black TiO<sub>2</sub> to cocatalyst-free hydrogen production. *ACS Catalysis*, 2019, 9(1): 345–364
- Moniz S J A, Shevlin S A, Martin D J, et al. Visible-light driven heterojunction photocatalysts for water splitting – a critical review. *Energy & Environmental Science*, 2015, 8(3): 731–759
- Yi S, Zhang X, Wulan B, et al. Non-noble metals applied to solar water splitting. *Energy & Environmental Science*, 2018, 11(11): 3128–3156
- Wang C, Li J, Paineau E, Laachachi A, et al. A sol-gel biotemplating route with cellulose nanocrystals to design a photocatalyst for improving hydrogen generation. *Journal of Materials Chemistry A*, 2020, 8(21): 10779–10786
- Wei L, Yu C, Zhang Q, et al. TiO<sub>2</sub>-based heterojunction photocatalysts for photocatalytic reduction of CO<sub>2</sub> into solar fuels. *Journal of Materials Chemistry A, Materials for Energy and Sustainability*, 2018, 6(45): 22411–22436
- Li J, Jiménez-Calvo P, Paineau E, et al. Metal chalcogenides based heterojunctions and novel nanostructures for photocatalytic hydrogen evolution. *Catalysts*, 2020, 10(1): 89
- Bessekhouad Y, Chaoui N, Trzpit M, et al. UV-vis versus visible degradation of Acid Orange II in a coupled CdS/TiO<sub>2</sub> semiconductors suspension. *Journal of Photochemistry and Photobiology A Chemistry*, 2006, 183(1–2): 218–224
- Xu D, Hai Y, Zhang X, et al. Bi<sub>2</sub>O<sub>3</sub> cocatalyst improving photocatalytic hydrogen evolution performance of TiO<sub>2</sub>. *Applied Surface Science*, 2017, 400: 530–536
- Lopes O F, Carvalho K T G, Avansi W Jr, et al. Growth of BiVO<sub>4</sub> nanoparticles on a Bi<sub>2</sub>O<sub>3</sub> surface: effect of heterojunction formation on visible irradiation-driven catalytic performance. *Journal of Physical Chemistry C*, 2017, 121(25): 13747–13756
- Wu Y, Lu G, Li S. The doping effect of Bi on TiO<sub>2</sub> for photocatalytic hydrogen generation and photodecolorization of rhodamine B. *Journal of Physical Chemistry C*, 2009, 113(22): 9950–9955
- Zhang L, Ye X, Boloor M, et al. Significantly enhanced photocurrent for water oxidation in monolithic Mo: BiVO<sub>4</sub>/SnO<sub>2</sub>/Si by thermally increasing the minority carrier diffusion length. *Energy & Environmental Science*, 2016, 9(6): 2044–2052
- Xie M, Fu X, Jing L, et al. Long-lived, visible-light-excited charge carriers of TiO<sub>2</sub>/BiVO<sub>4</sub> nanocomposites and their unexpected photoactivity for water splitting. *Advanced Energy Materials*, 2014, 4(5): 1300995
- Ho C H, Chan C H, Huang Y, et al. The study of optical band edge property of bismuth oxide nanowires α-Bi<sub>2</sub>O<sub>3</sub>. *Optics Express*,

- 2013, 21(10): 11965–11972
21. Bessekhoud Y, Robert D, Weber J V. Photocatalytic activity of Cu<sub>2</sub>O/TiO<sub>2</sub>, Bi<sub>2</sub>O<sub>3</sub>/TiO<sub>2</sub> and ZnMn<sub>2</sub>O<sub>4</sub>/TiO<sub>2</sub> heterojunctions. *Catalysis Today*, 2005, 101(3–4): 315–321
  22. Ayekoe P Y, Robert D, Goné D L. Preparation of effective TiO<sub>2</sub>/Bi<sub>2</sub>O<sub>3</sub> photocatalysts for water treatment. *Environmental Chemistry Letters*, 2016, 14(3): 387–393
  23. Reddy N L, Emin S, Valant M, et al. Nanostructured Bi<sub>2</sub>O<sub>3</sub>@TiO<sub>2</sub> photocatalyst for enhanced hydrogen production. *International Journal of Hydrogen Energy*, 2017, 42(10): 6627–6636
  24. Meng S, Sun W, Zhang S, et al. Insight into the transfer mechanism of photogenerated carriers for WO<sub>3</sub>/TiO<sub>2</sub> heterojunction photocatalysts: Is it the transfer of band-band or Z-scheme? Why? *Journal of Physical Chemistry C*, 2018, 122(46): 26326–26336
  25. Gesesse G D, Li C, Paineau E, et al. Enhanced photogenerated charge carriers and photocatalytic activity of biotemplated mesoporous TiO<sub>2</sub> films with a chiral nematic structure. *Chemistry of Materials*, 2019, 31(13): 4851–4863
  26. Chen M, Li Y, Wang Z, et al. Controllable synthesis of core-shell Bi@amorphous Bi<sub>2</sub>O<sub>3</sub> nanospheres with tunable optical and photocatalytic activity for NO removal. *Industrial & Engineering Chemistry Research*, 2017, 56(37): 10251–10258
  27. Ghazzal M N, Kebaili H, Joseph M, et al. Photocatalytic degradation of Rhodamine 6G on mesoporous titania films: combined effect of texture and dye aggregation forms. *Applied Catalysis B: Environmental*, 2012, 115–116: 276–284
  28. Ghazzal M N, Wojcieszak R, Raj G, et al. Study of mesoporous CdS-quantum-dot-sensitized TiO<sub>2</sub> films by using X-ray photoelectron spectroscopy and AFM. *Beilstein Journal of Nanotechnology*, 2014, 5: 68–76
  29. Sanna S, Esposito V, Andreasen J W, et al. Enhancement of the chemical stability in confined δ-Bi<sub>2</sub>O<sub>3</sub>. *Nature Materials*, 2015, 14(5): 500–504
  30. Jiang H Y, Cheng K, Lin J. Crystalline metallic Au nanoparticle-loaded α-Bi<sub>2</sub>O<sub>3</sub> microrods for improved photocatalysis. *Physical Chemistry Chemical Physics*, 2012, 14(35): 12114–12121
  31. Ghazzal M N, Chaoui N, Genet M, et al. Effect of compressive stress inducing a band gap narrowing on the photoinduced activities of sol-gel TiO<sub>2</sub> films. *Thin Solid Films*, 2011, 520(3): 1147–1154
  32. Nam H J, Amemiya T, Murabayashi M, et al. Photocatalytic activity of sol-gel TiO<sub>2</sub> thin films on various kinds of glass substrates: the effects of Na<sup>+</sup> and primary particle size. *Journal of Physical Chemistry B*, 2004, 108(24): 8254–8259
  33. Xu Y, Schoonen M A A. The absolute energy positions of conduction and valence bands of selected semiconducting minerals. *American Mineralogist*, 2000, 85(3–4): 543–556
  34. Savenije T J, Ferguson A J, Kopidakis N, et al. Revealing the dynamics of charge carriers in polymer: fullerene blends using photoinduced time-resolved microwave conductivity. *Journal of Physical Chemistry C*, 2013, 117(46): 24085–24103